Tunable Correlated States and Spin-polarized Phases in Twisted Bilayer-Bilayer Graphene

Yuan Cao[1,*], Daniel Rodan-Legrain[1], Oriol Rubies-Bigorda[1], Jeong Min Park[1], Kenji Watanabe[2], Takashi Taniguchi[2], Pablo Jarillo-Herrero[1,†]

[1]Department of Physics, Massachusetts Institute of Technology, Cambridge, Massachusetts 02139, USA

[2]National Institute for Materials Science, Namiki 1-1, Tsukuba, Ibaraki 305-0044, Japan

[*]caoyuan@mit.edu

[†]pjarillo@mit.edu

The recent discovery of correlated insulator states and superconductivity in magic-angle twisted bilayer graphene (TBG) [1,2] has paved the way to the experimental investigation of electronic correlations in tunable flat band systems realized in twisted van der Waals heterostructures [3–6]. This novel twist angle degree of freedom and control should be generalizable to other 2D systems, which may exhibit similar correlated physics behaviour as well as enable new techniques to tune and control the strength of electron-electron interactions. Here, we report on a novel highly tunable correlated system based on small-angle twisted bilayer-bilayer graphene (TBBG), consisting of two rotated sheets of Bernal-stacked bilayer graphene. We find that TBBG exhibits a rich phase diagram, with tunable correlated insulators states that are highly sensitive to both twist angle and to the application of an electric displacement field, the latter reflecting the inherent polarizability of Bernal-stacked bilayer graphene [7,8]. The correlated insulator states can be switched on and off by the displacement field at all integer electron fillings of the moiré unit cell. The response of these correlated states to magnetic fields suggests evidence of spin-polarized ground states, in stark contrast to magic-angle TBG. Furthermore, in the regime of lower twist angles, TBBG shows multiple sets of flat bands near charge neutrality, resulting in numerous correlated states corresponding to half-filling of each of these flat bands, all of which are tunable by the displacement field as well. Our results pave the way to the exploration of novel twist-angle and electric-field controlled correlated phases of matter in novel multi-flat band twisted superlattices.

Electronic correlations play a fundamental role in condensed matter systems where the bandwidth is comparable to or less than the Coulomb energy between electrons. These correlation effects often manifest themselves as intriguing quantum phases of matter, such as ferromagnetism, superconductivity, Mott insulators, or fractional quantum Hall states. Understanding, predicting, and characterizing these correlated phases is of great interest in modern condensed matter physics research and pose challenges to both experimentalists and theorists. Recent studies in twisted graphene superlattices provide us with an ideal tunable platform to investigate electronic correlations in two dimensions [1,2,9–11]. Tuning the twist angle of 2D van der Waals heterostructures to realize novel electronic states, an emerging field referred to as 'twistronics', has enabled physicists to explore a variety of novel phenomena. [12–16]. When two layers of graphene are twisted by a specific angle, the phase diagram in the system exhibits correlated insulator states with similarities to Mott insulator systems[1,17], as well as unconventional superconducting states upon charge doping[2,9,11,18]. These effects are likely to originate from the many-body interactions between the electrons, when the band structure becomes substantially narrow as the twist angle approaches the first magic angle θ=1.1°. [3–5]

Here we extend the twistronics research on graphene superlattices to a novel system with electrical displacement field tunability --- twisted bilayer-bilayer graphene (TBBG), which consists of two sheets of untwisted Bernal-stacked bilayer graphene stacked together at an angle θ, as illustrated in Fig. 1a. The band structure of bilayer graphene is highly sensitive to the applied perpendicular electric displacement field [7,19,20], and therefore provides us with an extra knob to control the relative strength of electronic correlations in the bands[17]. Similar to TBG[3–5], the band structure of TBBG is flattened near ~1.1° (see Fig. 2e-g)[21]. For devices with twist angle near this value, our experiments show that the correlated insulator behaviour at $n_s/2$, $n_s/4$, and $3n_s/4$ can be sensitively turned on and off by the displacement field, where n_s is the density corresponding to fully filling one spin and valley degenerate superlattice band[22,23]. From their response to magnetic fields, all of these correlated states likely have a spin-polarized nature, with the $n_s/2$ state having a g-factor of ~1.5 for parallel fields, close to the bare electron spin g-factor of 2. On the other hand, devices with a smaller twist angle of 0.84° display multiple displacement field tunable correlated states at higher fillings, consistent with the presence of several sets of correlated flat bands in the electronic structure. The combination of twist angle, electric displacement field, and magnetic field provides a rich arena to investigate novel correlated phenomena in the emerging field of twistronics.

We fabricated high-mobility dual-gated TBBG devices with the reported ‘tear and stack’ method[22,23], using exfoliated Bernal-stacked bilayer graphene instead of monolayer graphene. The devices presumably have an AB-AB stacking configuration where the top and bottom bilayers retain the same AB stacking order, in contrast to the AB-BA structure that was predicted to show topological effects [24]. We measured the transport properties of six small-angle devices, and here we focus on three of the devices with twist angles θ=1.23°, 1.09° and 0.84° respectively (see Extended Data Figure 1 for other devices). The samples are all of high quality, as evident in the Landau fan diagrams, with Hall mobilities that can exceed 100,000 $\mathrm{cm}^2/(\mathrm{V}\cdot\mathrm{s})$, shown in Extended Data Figure 2. Figures 1c-e show the longitudinal resistance R_{xx} and the low-field Hall coefficient R_H=dR_{xy}/dB versus charge density for these three devices at T=4 K. In a superlattice, the electronic band structure is folded in the mini Brillouin zone (MBZ), defined by the moiré periodicity[4]. Each band in the MBZ can accommodate a total charge density of n_s=4/A, where A is the size of the moiré unit cell and the pre-factor accounts for spin and valley degeneracies[4,21,22]. The experimental results show a sign change in the Hall coefficient R_H at each multiple of n_s (vertical dashed lines in Fig. 1c-e), indicating the switching of hole-like pockets to electron-like pockets, and peaks in R_{xx}, indicating the crossing of new band edges (for θ=0.84°, the band edges at -n_s and ±2n_s may only have small gaps or may even be semi-metallic, and hence do not exhibit prominent peaks in R_{xx}. See Fig. 4a-b for band structure calculations). The sharpness of the peaks confirms that the devices exhibit relatively low disorder and have well-defined twist angles.

In the θ=1.23° and θ=1.09° devices, we observe signatures of newly formed gaps at n_s/2 when a displacement field D is applied perpendicular to the device. The dual-gate device geometry allows us to independently vary the total charge density n and D (see Methods for details of the transformation between gate voltages and (n, D)). Fig. 1f shows the resistance map in the V_{tg}-V_{bg} space for the θ=1.09° device. At D=0, no insulating behaviour other than the full-filling gaps at ±n_s is observed. However, when a displacement field D is applied in either direction, an insulating state appears at n_s/2 for a range of |D|. This new insulating state induced by the displacement field is further examined by measuring the Hall coefficient R_H versus n and D, as shown in the left panel of Fig. 1g (θ=1.09° device), and comparing with R_{xx} shown in the right panel. At the onset of the insulating states at $D/\varepsilon_0\approx\pm0.18$ V/nm, where ε_0 is the vacuum permittivity, R_H develops additional sign changes adjacent to the insulating states, suggesting the creation of new gaps by the displacement field. The insulating states disappear when D/ε_0 exceeds ±0.35 V/nm. In both the θ=1.09° device and the θ=1.23° devices, we find signatures of the onset of correlated behaviour at n=-n_s/2, D=0, but no well-developed insulating state is observed (see Extended Data Figure 1 and Methods).

In the θ=1.23° device, we observe a similar but more intricate hierarchy of tunable insulating states that stem from the interplay of correlations, the superlattice bands, and the magnetic field. Fig. 2a shows the n-D resistance map for the θ=1.23° TBBG device measured at T=0.07 K. Noticeably, as $|D|$ is increased the insulating state at charge neutrality n=0 strengthens in the same way as in the Bernal-stacked bilayer graphene[7,19,20], while the superlattice gaps at $\pm n_s$ weaken and eventually disappear (at $|D|/\varepsilon_0$>0.6 V/nm for the $+n_s$ insulating state and at $|D|/\varepsilon_0$>0.35 V/nm for the $-n_s$ insulating state). The band structures of TBBG in zero and finite external displacement fields calculated using a continuum approximation are shown in Fig. 2e-g (see Methods for details). It should be noted that, although TBBG has twice the number of graphene layers than TBG, the band counting is the same, *i.e.* each band (spin/valley degenerate) accommodates 4 electrons per moiré unit cell. At zero displacement field, the calculated gap at the charge neutrality is negligible, while the superlattice gaps above and below the flat bands are nonzero. When the displacement field is increased, the charge neutrality gap quickly widens while the superlattice gaps become smaller and eventually vanish, in agreement with our experimental observations.

At intermediate displacement fields around D/ε_0=-0.38 V/nm, we observe the insulating states not only at n_s/2 over a wider range of D, but also at n_s/4 over a smaller range (Fig. 2a). We attribute these states to a Mott-like mechanism similar to those observed in TBG, which results from the Coulomb repulsion of the electrons in the flat bands when each unit cell hosts exactly 1 or 2 electrons, corresponding to n_s/4 and n_s/2 fillings respectively. The n_s/4 state requires a finer tuning of D to reveal, possibly due to the smaller gap size. This is evident from Fig. 2b, where we show the resistance versus n and temperature T with the displacement field D/ε_0 fixed at -0.38 V/nm. While the n_s/2 state persists up to approximately 8 K, the n_s/4 state disappears at less than 3 K, indicating a smaller gap. Fig. 2c shows the resistance of the n_s/2 state versus the displacement field and temperature. The 'optimal' displacement field to reach the maximal resistance is approximately ±0.4 V/nm. As the temperature increases, the peak in R_{xx} not only decreases in value but also broadens in D. In the inset, we show the evolution of the gap versus the displacement field. At temperatures higher than 10 K and away from the charge neutrality point, the transport is dominated by a linear R-T behaviour similar to that observed in TBG (Fig. 2d, see also Extended Data Figure 3 and Methods). [2,9,25,26]

Figure 3 shows the response of the various correlated states to magnetic fields in perpendicular or in-plane direction with respect to the sample plane. Figures 3a-c show the *n*-*D* maps of the resistance for the θ=1.23° device at B=0 T, $B_{\perp}$=8 T and $B_{\parallel}$=8 T, respectively. The plots focus on densities from n=0 to $n=n_s$. Fig 3a shows the band insulator states at n=0 and $n=n_s$, as well as the correlated insulating states at $n_s/2$ and $n_s/4$ (encircled by dashed lines), but not at $3n_s/4$ filling at this zero magnetic field. Interestingly, at $B_{\perp}$=8 T (Fig. 3b), the correlated insulating states at $n_s/4$ and $n_s/2$ vanish at their original positions centered around D/ε_0=-0.38 V/nm, whereas new insulating states appear at $n=n_s/4$, D/ε_0=-0.2~-0.35 V/nm and $n=n_s/2$, D/ε_0=-0.45~-0.6 V/nm, above and below their original positions at B=0 respectively. A new correlated insulating state also now appears at $3n_s/4$, D/ε_0=-0.4~-0.5 V/nm. However, no such strong shift is observed with in-plane magnetic field (Fig. 3c). At $B_{\parallel}$=8 T, the correlated insulating states are clearly visible at all integer electron fillings ($n_s/4$, $n_s/2$, $3n_s/4$) near D/ε_0=-0.38 V/nm. Figures 3d-e show the evolution of the $n_s/2$ insulating state as a function of $B_{\perp}$ and $B_{\parallel}$. An abrupt shift in the range of D for which the insulating state appears occurs at $B_{\perp}$=5 T, whereas the insulating state strengthens monotonically with in-plane magnetic field.

The key difference between the effects of the perpendicular and in-plane magnetic fields lies in the fact that the lateral dimension of the unit cell in TBBG, ~10 nm, is much larger than the thickness of the system ~1 nm. Therefore, while both fields couple equally to the spins of the correlated electrons, $B_{\parallel}$ has a much weaker (but nonzero) effect on the orbital movement of the electrons. To theoretically understand the behaviour of the correlated insulating states in a magnetic field, we first have to identify their ground state. Figures 3f-g show the evolution of the thermal activation gap of the $n_s/2$ state in both $B_{\perp}$ and $B_{\parallel}$. We find a g-factor of $g_{\perp}$~3.5 for the perpendicular direction (up to 5 T before the shift occurs) and a g-factor of $g_{\parallel}$~1.5 for the in-plane direction. $g_{\parallel}$ is close to (but less than) g=2, which is expected for a spin-polarized ground state with contribution only from the electron spins. This difference is theoretically expected because of finite in-plane orbital effects[27]. Therefore, based on these measurements, we may conclude that the correlated insulating states have a spin-polarized nature. These observations establish TBBG as a distinctive system from the previously reported magic-angle TBG system [1,2,9], which exhibits half-filling insulating states that are shown to be spin unpolarized, as they are suppressed by an in-plane magnetic field. In $B_{\perp}$, on the other hand, one would expect orbital effects to play a more substantial role. We may attribute the larger $g_{\perp}$ of about 3.5 to exchange-induced enhancement effects, similar to what is observed in Landau levels of GaAs quantum wells and graphene [28,29]. In Extended Data Figure 4, we provide additional magnetic field response data for the $n_s/4$ and the $3n_s/4$ states. Both of these states also exhibit a spin-polarized behaviour, as they become more resistive under the in-plane magnetic field.

In addition to the discussion above, we noticed that all the correlated insulating states in the θ=1.23° TBBG device, whether at zero magnetic field or high magnetic fields, lie within the range D/ε_0=-0.6 ~ -0.2 V/nm. Coincidentally, this is also the range where both the gap at the charge neutrality (n=0) and the gap at the superlattice density ($n=n_s$) are well-developed (*i.e.* the case in Fig. 2f). Based on this observation, we suggest that the displacement field tunability of the correlated states is tied to the modulation of the single-particle band gaps by the displacement field[27]. When either gap at n=0 or $n=n_s$ is absent, the thermally excited or disorder scattered carriers from the upper or lower band would suppress the ordering of the electrons and hence the correlated states. Further theoretical work is needed to reveal the detailed structure of the displacement field dependence of the correlated states.

We have also investigated the regime of substantially smaller twist angles. Unlike the case of TBG, further reduction of the twist angle of TBBG to 0.84° results not in one, but rather three pairs of flat bands, separated from other bands by band gaps (Fig. 4a). Application of an electrical displacement field further flattens these bands and separate them from each other (Fig. 4b). This would imply that all electrons within the density range $-3n_s$ to $+3n_s$ might experience strong Coulomb interactions, and their correlations can get further enhanced by applying a displacement field. These predictions from the band theory are consistent with our experimental observations. In Fig. 4c where we show the resistance map of the θ=0.84° TBBG device versus n and D, we indeed find that the weak signatures of $-n_s/2$ and $-n_s/4$ correlated insulating states only appear at high displacement fields $|D|/\varepsilon_0 > 0.4$ V/m (encircled by white dashed lines). The full-filling gaps at $\pm n_s$ and $\pm 2n_s$ are tunable by the displacement field to different extents as well.

As we turn on a perpendicular magnetic field, a series of correlated insulator states appear across the entire density range spanning the multiple flat bands. Figures 4d and 4e show the Landau fan diagrams at D/ε_0=0.6 V/m and D=0 respectively. At zero displacement field, the Landau fan shows a complicated Hofstadter butterfly pattern due to commensurate flux threading into the unit cell [12–14] (see also Methods and Extended Data Figure 2), but no correlated state is observed at half-fillings or quarter-fillings. We note that a resistive region appears at $n \approx 1.63n_s$ in Fig. 4e, which does not coincide with any commensurate filling and might be ascribed to twist angle inhomogeneity in the sample. On the other hand, at D/ε_0 =0.6 V/nm, we find clear signatures of correlated states at $n_s/2$ and $-n_s/2$ in the center flat bands, and weak evidences at $3n_s/2$ and $5n_s/2$ in the upper flat bands. All of these half-filling correlated states appear to be enhanced by the application of a perpendicular magnetic field, which we attribute to the same spin/orbital combined enhancement of the correlated gaps as in the $n_s/2$ state of the θ=1.23° device (see Fig. 3f). The correlated states at $\pm n_s/2$ appear to be significantly stronger than the states at $3n_s/2$ and $5n_s/2$ in high magnetic fields, consistent with the fact that from our calculations the pair of bands closer to charge neutrality is much flatter than the other two pairs farther away from charge neutrality, as can be seen in Fig. 4b. The resistance of the quarter-filling state at $n_s/4$, however, does not increase monotonically with perpendicular field, but rather eventually gets suppressed at 5 T.

Our results show that TBBG exhibits a rich spectrum of correlated phases tunable by twist angle, electric displacement field, and magnetic field, paving the way to further studies of strongly correlated physics and topology in multi-flat band systems[21].

References

1. Cao, Y. *et al.* Correlated insulator behaviour at half-filling in magic-angle graphene superlattices. *Nature* **556**, 80–84 (2018).
2. Cao, Y. *et al.* Unconventional superconductivity in magic-angle graphene superlattices. *Nature* **556**, 43–50 (2018).
3. Suárez Morell, E., Correa, J. D., Vargas, P., Pacheco, M. & Barticevic, Z. Flat bands in slightly twisted bilayer graphene: Tight-binding calculations. *Phys. Rev. B* **82**, 121407 (2010).
4. Bistritzer, R. & MacDonald, A. H. Moiré bands in twisted double-layer graphene. *Proc. Natl. Acad. Sci.* **108**, 12233–12237 (2011).

5. Lopes dos Santos, J. M. B., Peres, N. M. R. & Castro Neto, A. H. Continuum model of the twisted graphene bilayer. *Phys. Rev. B* **86**, 155449 (2012).
6. Carr, S. *et al.* Twistronics: Manipulating the electronic properties of two-dimensional layered structures through their twist angle. *Phys. Rev. B* **95**, 075420 (2017).
7. McCann, E. & Koshino, M. The electronic properties of bilayer graphene. *Rep. Prog. Phys.* **76**, 056503 (2013).
8. Castro Neto, A. H., Guinea, F., Peres, N. M. R., Novoselov, K. S. & Geim, A. K. The electronic properties of graphene. *Rev. Mod. Phys.* **81**, 109–162 (2009).
9. Yankowitz, M. *et al.* Tuning superconductivity in twisted bilayer graphene. *Science* **363**, 1059–1064 (2019).
10. Sharpe, A. L. *et al.* Emergent ferromagnetism near three-quarters filling in twisted bilayer graphene. *Science* **365**, 605–608 (2019).
11. Lu, X. *et al.* Superconductors, orbital magnets and correlated states in magic-angle bilayer graphene. *Nature* **574**, 653–657 (2019).
12. Hunt, B. *et al.* Massive Dirac Fermions and Hofstadter Butterfly in a van der Waals Heterostructure. *Science* **340**, 1427–1430 (2013).
13. Ponomarenko, L. A. *et al.* Cloning of Dirac fermions in graphene superlattices. *Nature* **497**, 594–597 (2013).
14. Dean, C. R. *et al.* Hofstadter's butterfly and the fractal quantum Hall effect in moiré superlattices. *Nature* **497**, 598–602 (2013).
15. Kumar, R. K. *et al.* High-temperature quantum oscillations caused by recurring Bloch states in graphene superlattices. *Science* **357**, 181–184 (2017).
16. Li, G. *et al.* Observation of Van Hove singularities in twisted graphene layers. *Nat. Phys.* **6**, 109–113 (2010).
17. Chen, G. *et al.* Evidence of a gate-tunable Mott insulator in a trilayer graphene moiré superlattice. *Nat. Phys.* **15**, 237 (2019).
18. Chen, G. *et al.* Signatures of tunable superconductivity in a trilayer graphene moiré superlattice. *Nature* **572**, 215–219 (2019).
19. Oostinga, J. B., Heersche, H. B., Liu, X., Morpurgo, A. F. & Vandersypen, L. M. K. Gate-induced insulating state in bilayer graphene devices. *Nat. Mater.* **7**, 151–157 (2008).
20. Zhang, Y. *et al.* Direct observation of a widely tunable bandgap in bilayer graphene. *Nature* **459**, 820–823 (2009).
21. Zhang, Y.-H., Mao, D., Cao, Y., Jarillo-Herrero, P. & Senthil, T. Nearly flat Chern bands in moiré superlattices. *Phys. Rev. B* **99**, 075127 (2019).

22. Cao, Y. *et al.* Superlattice-Induced Insulating States and Valley-Protected Orbits in Twisted Bilayer Graphene. *Phys. Rev. Lett.* **117**, 116804 (2016).
23. Kim, Y. *et al.* Charge Inversion and Topological Phase Transition at a Twist Angle Induced van Hove Singularity of Bilayer Graphene. *Nano Lett.* **16**, 5053–5059 (2016).
24. Koshino, M. Band structure and topological property of twisted double bilayer graphenes. *Phys. Rev. B* **99**, 235406 (2019).
25. Polshyn, H. *et al.* Large linear-in-temperature resistivity in twisted bilayer graphene. *Nat. Phys.* **15**, 1011–1016 (2019).
26. Cao, Y. *et al.* Strange metal in magic-angle graphene with near Planckian dissipation. *ArXiv190103710 Cond-Mat* (2019).
27. Lee, J. Y. *et al.* Theory of correlated insulating behaviour and spin-triplet superconductivity in twisted double bilayer graphene. *Nat. Commun.* **10**, 5333 (2019).
28. Raymond, A. *et al.* Gigantic exchange enhancement of spin g-factor for two-dimensional electron gas in GaAs. *Solid State Commun.* **55**, 271–274 (1985).
29. Young, A. F. *et al.* Spin and valley quantum Hall ferromagnetism in graphene. *Nat. Phys.* **8**, 550–556 (2012).

Acknowledgements

We acknowledge helpful discussions with S. Todadri, L. Fu, P. Kim, X. Liu, S. Fang and E. Kaxiras. This work has been supported by the National Science Foundation under award DMR-1809802 (data analysis by Y.C.), the Center for Integrated Quantum Materials under NSF grant DMR-1231319 (fabrication by D.R-L.), the US DOE, BES Office, Division of Materials Sciences and Engineering under Award DE-SC0001819 (g-factor analysis by J.M.P.), and the Gordon and Betty Moore Foundation's EPiQS Initiative through Grant GBMF4541 to P.J-H. K.W. and T.T. acknowledge support from the Elemental Strategy Initiative conducted by the MEXT, Japan, A3 Foresight by JSPS and the CREST (JPMJCR15F3), JST. This work made use of the Materials Research Science and Engineering Center Shared Experimental Facilities supported by the National Science Foundation (DMR-0819762) and of Harvard's Center for Nanoscale Systems, supported by the NSF (ECS-0335765). D.R.-L. acknowledges partial support from Fundació Bancaria “la Caixa” (LCF/BQ/AN15/10380011) and from the US Army Research Office grant no. W911NF-17-S-0001 (measurements). O.R.-B. acknowledges support from Fundació Privada Cellex.

Author Contributions

Y.C., D.R-L., O.R-B. and J.M.P contributed to sample fabrication and transport measurements. Y.C., D.R-L., O.R-B., J.M.P and P.J-H. performed data analysis. K.W. and T.T. provided h-BN samples. Y.C., D.R-L., O.R-B., J.M.P. and P.J-H. wrote the manuscript with input from all co-authors.

Author Information

The authors declare no competing financial interest.

Additional Information

Correspondence and requests for materials should be addressed to caoyuan@mit.edu and pjarillo@mit.edu.

Figure Legends

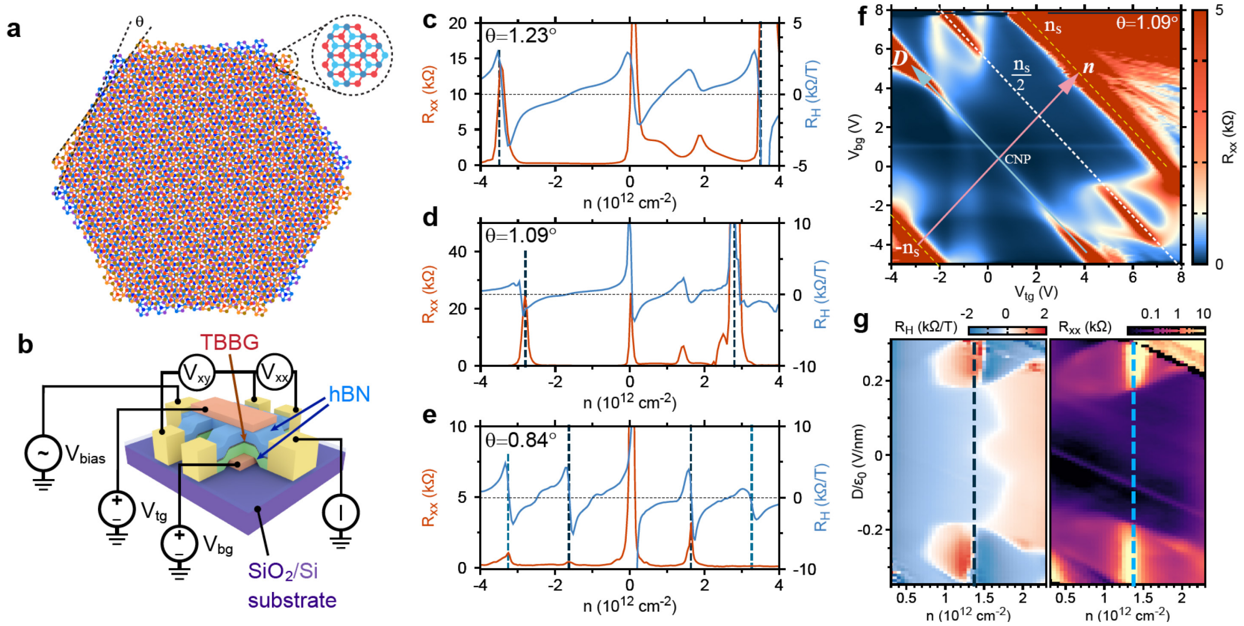

Figure 1. **Structure and transport characterization of twisted bilayer-bilayer graphene (TBBG)**. (a) TBBG consists of two sheets of Bernal-stacked bilayer graphene twisted at an angle θ. (b) Schematic of a typical TBBG device with top and bottom gates and a Hall-bar geometry for transport measurements. (c-e) Measured longitudinal resistance $R_{xx}=V_{xx}/I$ and low-field Hall coefficient $R_H=d/dB(V_{xy}/I)$ as functions of carrier density n in three devices with twist angles θ=1.23°, 1.09° and 0.84° respectively. The vertical dashed lines denote multiples of the superlattice density n_s, where the peaking of R_{xx} and sign changing of R_H indicate the Fermi energy crosses a band edge of the superlattice bands. (f) Resistance of the 1.09° TBBG device versus both top gate and bottom gate voltages V_{tg} and V_{bg}. The charge density n and displacement field D are related to the gate voltages by a linear transformation (see Methods). The superlattice densities $\pm n_s$ and the half-filling at $n_s/2$ are indicated by dashed lines parallel to the D axis. Correlated insulator states are observed at $n_s/2$ filling in finite displacement fields. (g) Map of low-field Hall coefficient R_H (left panel) and resistance R_{xx} (right panel) near the $n_s/2$ correlated states for the 1.09° TBBG device (the vertical dashed lines indicate $n_s/2$). We find that accompanying the onset of the correlated insulator states at $D/\varepsilon_0 \approx \pm 0.18$ V/nm, a new sign change of the Hall coefficient also emerges.

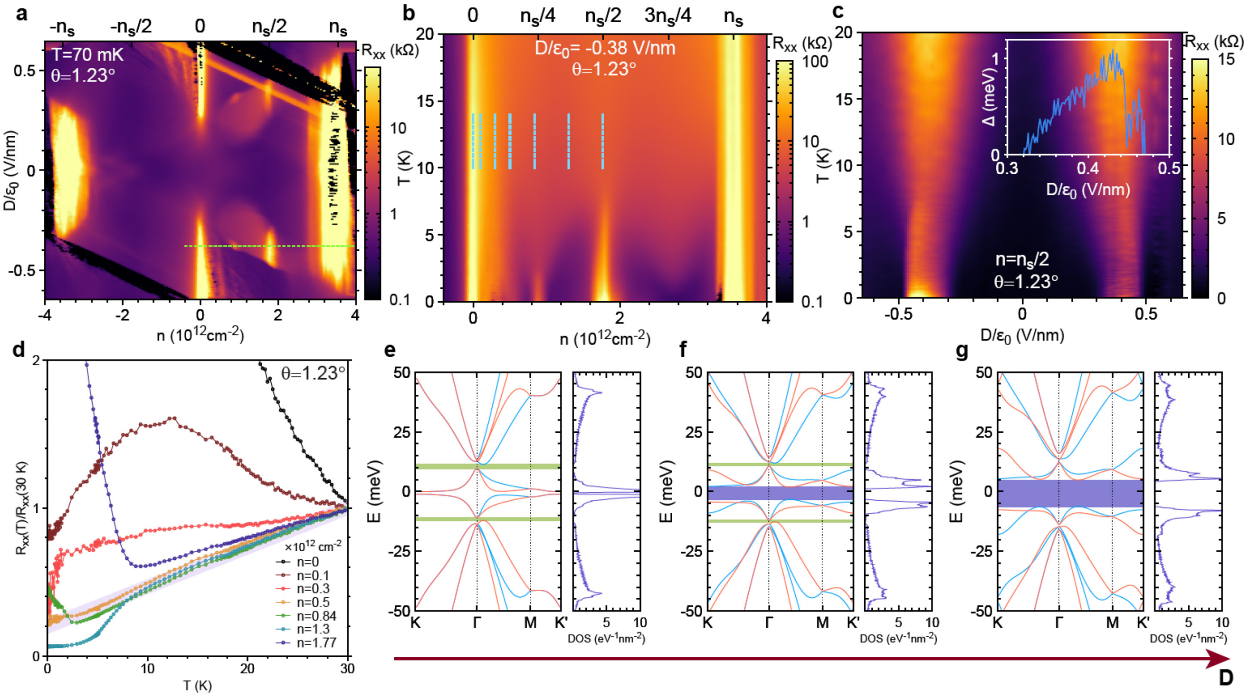

Figure 2. **Displacement field tunable correlated insulator states in TBBG.** (a) Color plot of resistance versus charge density n and displacement field *D* (θ=1.23° device, section 1, see Methods). The green dashed line cutting through the *D*<0 correlated state is the linecut along which (b) is taken (for θ=1.23° device, section 2, see Methods) (b) Resistance versus *n* and *T* at a fixed D/ε_0=-0.38 V/nm. The correlated insulator states at $n_s/4$ and $n_s/2$ are suppressed by raising the temperature. (c) Resistance at density $n_s/2$ versus displacement field and temperature. The resistance shows a maximum at approximately D/ε_0=±0.4 V/nm, the region where the correlated insulator state is present. The inset shows the thermal activation gap extracted from temperature dependence at different values of D across the $n_s/2$ state. (d) Normalized resistance curves versus temperature at various densities between 0 and $n_s/2 \approx 1.77\times10^{12}$ cm^{-2}, which are indicated by dashed lines in (b). Away from the charge neutrality point, all resistance curves show approximately linear *R*-*T* behaviour above 10 K, with similar slopes (see Extended Data Figure 3). (e-g) Calculated band structure (left panels) and density of states (right panels) for θ=1.23° TBBG at (e) ΔV=0, (f) ΔV=6 mV and (g) ΔV=12 mV, where ΔV is the potential difference between adjacent graphene layers induced by the external displacement field (assumed to be the same between all layers). Single-particle bandgaps in the dispersion are highlighted by green (below and above the flat bands) and blue (at charge neutrality) bars.

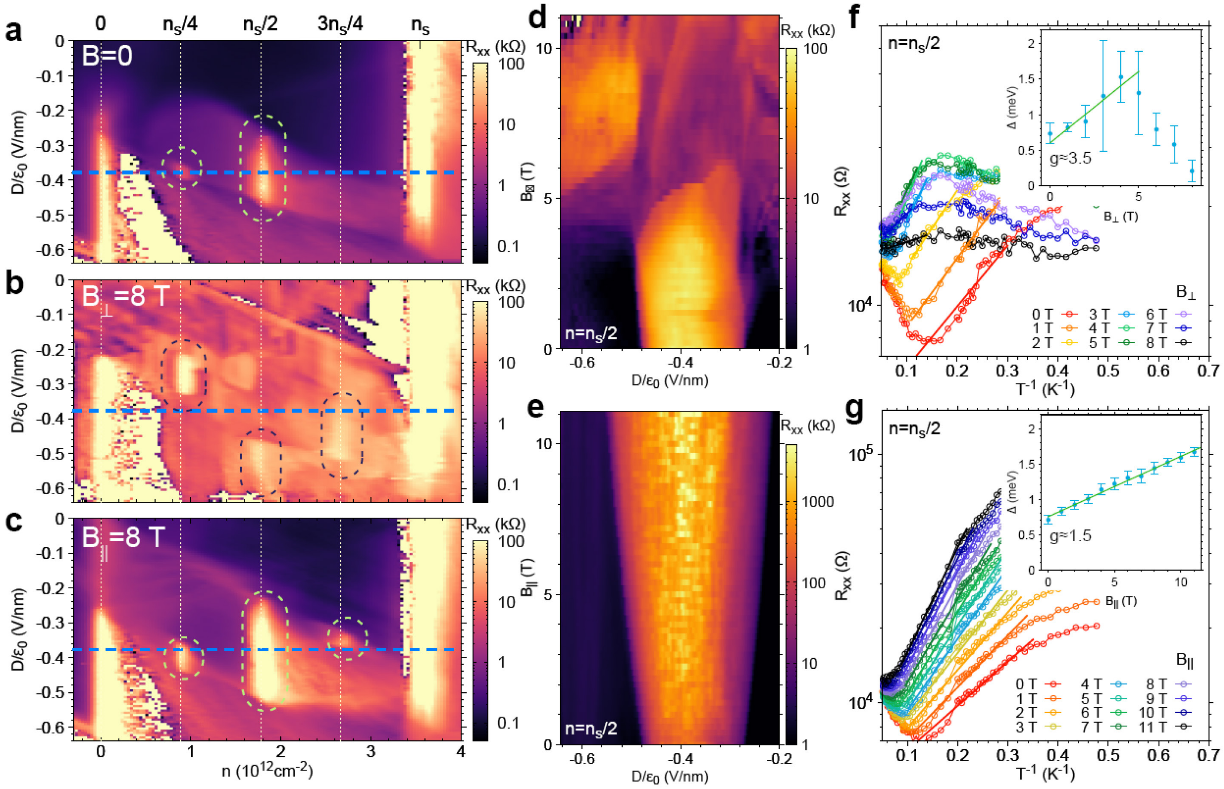

Figure 3. **Magnetic field response of the displacement-field-tunable correlated insulator states in TBBG.** (a-c) Resistance plot for the θ=1.23° TBBG device in magnetic fields of B=0, $B_\perp$=8 T perpendicular to the sample, and $B_\parallel$=8 T parallel to the sample, respectively. All measurements are taken at sample temperature T=0.07 K. Various correlated states at integer electron fillings of the moiré unit cell are indicated by dashed circles. At zero field, only the $n_s/4$ and $n_s/2$ states appear around $|D|/\varepsilon_0$=0.38 V/nm. In a perpendicular field of 8 T, the $n_s/4$ state shifts towards lower $|D|$, the $n_s/2$ state shifts towards higher $|D|$, and a $3n_s/4$ state also emerges. In a parallel field of 8 T, on the other hand, the position of the states barely shifts but their resistance increases monotonically. (d-e) Resistance at $n=n_s/2$ versus displacement field and magnetic field applied (d) perpendicular and (e) in-plane with respect to the device. While the correlated insulator state monotonically strengthens in $B_\parallel$, the perpendicular field induces a phase transition at around $B_\perp$=5 T, where the correlated state abruptly shifts to higher $|D|$. (f-g) Temperature dependence of the resistance at the $n_s/2$ insulator in different magnetic fields, perpendicular in (f) and in-plane in (g). The insets show the thermal activation gaps extracted from the Arrhenius fits ($R \sim e^{-\frac{\Delta}{2k_BT}}$, where k_B is the Boltzmann constant) in the main figures (solid lines) versus the magnitude of the field in the respective orientation. Error bars correspond to a confidence level

of 0.99. The linear fit of the thermal activation gap gives a *g*-factor of about 3.5 for perpendicular field (up to 5 T only) and 1.5 for in-plane field (entire field range).

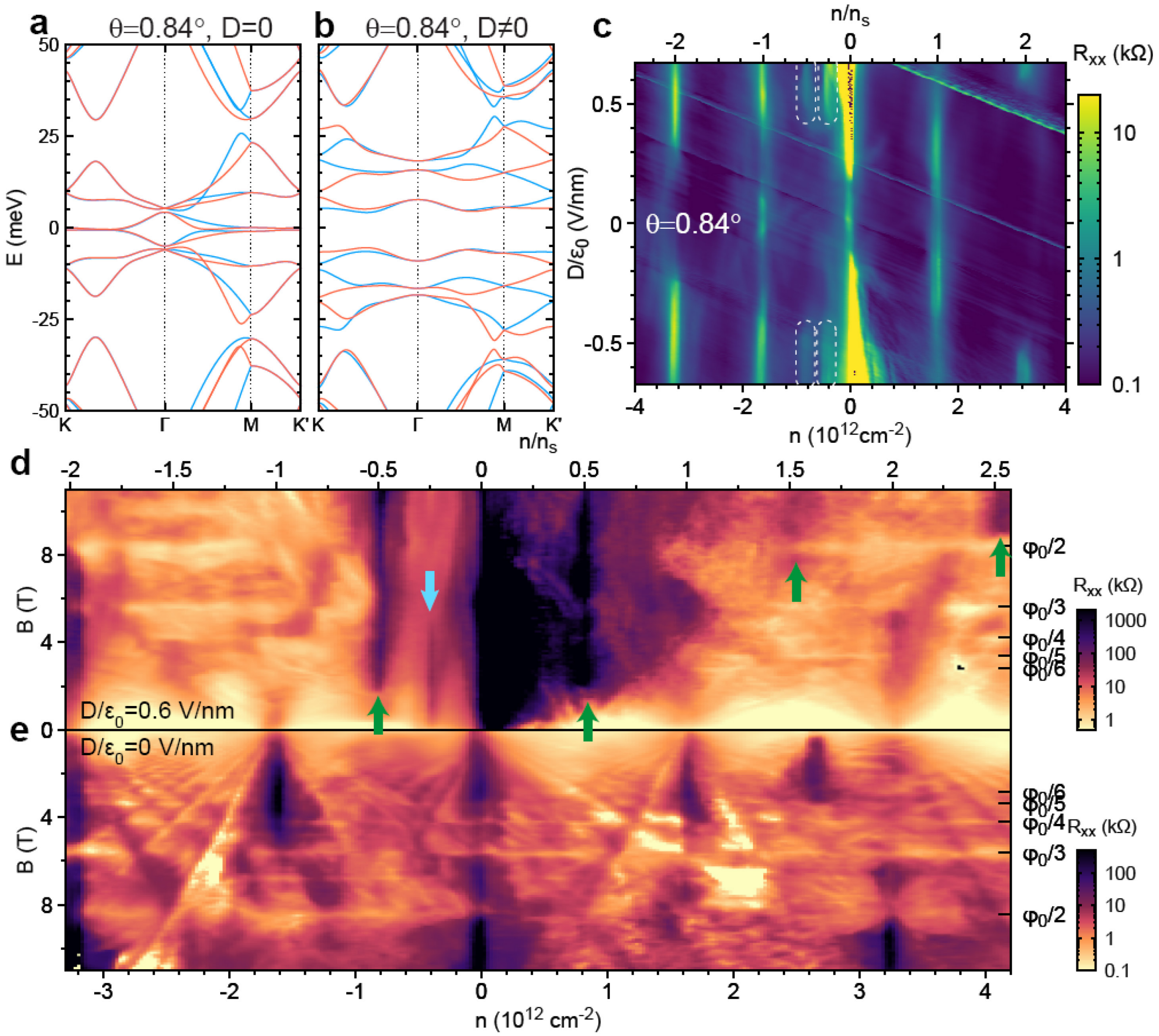

Figure 4. **Correlated insulator states in a multi flat band system.** (a-b) Calculated band structure of θ=0.84° TBBG (a) without interlayer potential and (b) with interlayer potential ΔV=18 mV. Near charge neutrality, within a 50 meV window, there are in total six sets of flat bands spanning densities -3n_s to 3n_s. Upon applying a displacement field, these bands are further flattened and separated from each other, which makes them more prone to giving rise to correlated states at each half-filling. (c) Resistance map of a θ=0.84° TBBG device measured at T=0.07 K. The top axis is the charge density normalized to the superlattice density n_s. Besides the D-tunable gaps at multiples of n_s, we find signatures of correlated states at n/n_s=-1/2, -1/4 for $|D|/\varepsilon_0 > 0.4$ V/nm, which are indicated by dashed circles. (d) Resistance as a function of charge density and perpendicular magnetic field B when a displacement is present, D/ε_0=0.6 V/nm. We find clear correlated states at

n/n_s=-1/2, 1/4 and 1/2, and also evidences at 3/2 and 5/2 fillings, as indicated by arrows. (e) For comparison, when no displacement field is present, we do not find any signature of half-filling correlated states. Due to the formation of a superlattice, we also observe Hofstadter butterfly related features when B is such that the magnetic flux in each unit cell is equal to $\varphi_0/2$, $\varphi_0/3$, $\varphi_0/4$, etc., where $\varphi_0=h/e$ is the flux quantum.

Methods

Fabrication and Measurement

The reported devices are fabricated with two sheets of Bernal-stacked bilayer graphene (BLG) and encapsulated by two hBN flakes. Both BLG and hBN were exfoliated on SiO_2/Si substrates, and the thickness and quality of the flakes were confirmed with optical microscopy and atomic force microscopy. A modified polymer-based dry pick-up technique was used for the fabrication of the heterostructures. A poly(bisphenol A carbonate) (PC) / polydimethylsiloxane (PDMS) layer on a glass slide was positioned in the micro-positioning stage to first pick up an hBN flake at ~100 °C. The van der Waals interaction between the hBN and BLG then allowed us to tear the BLG flake, which was then rotated at a desired angle and stacked at room temperature. The resulting hBN/BLG/BLG heterostructure was released on another hBN flake on a Pd/Au back gate that was pre-heated to 170 °C, using a hot transfer [30,31]. The desired geometry of the four-probe devices was achieved with electron beam lithography and reactive ion etching. The electrical contacts and top gate were deposited by thermal evaporation of Cr/Au, making edge contacts to the encapsulated graphene[32].

Electronic transport measurements were performed in a dilution refrigerator with a superconducting magnet, with a base electronic temperature of 70 mK. The data were obtained with low-frequency lock-in techniques. We measured the current through the sample amplified by 10^7 V/A and the four-probe voltage amplified by 1000, using SR-830 lock-in amplifiers that were all synchronized to the same frequency between 1~20 Hz. For resistance measurements we typically use a voltage excitation of <100 μV or current excitation of <10 nA.

List of Measured TBBG Devices

Following the definition given in the main text and accounting for offsets in the gate voltages due to impurity doping, n and D are related to the top and bottom gate voltages V_{tg} and V_{bg} by

$$n = [c_{tg}(V_{tg} - V_{tg,0}) + c_{bg}(V_{bg} - V_{bg,0})]/e$$

$$D = [-c_{tg}(V_{tg} - V_{tg,0}) + c_{bg}(V_{bg} - V_{bg,0})]/2$$

Extended Data Table 1 lists the twist angles and parameters c_{tg}, c_{bg}, $V_{tg,0}$, $V_{bg,0}$, and n_s for all devices discussed in this work, including those shown in the Extended Data Figures. These parameters are estimated to satisfy that all diagonal features in the $V_{tg} - V_{bg}$ maps are rotated to be vertical in the corresponding $n - D$ maps, and the features should be symmetrical with respect to D after the transformation.

In Extended Data Figures 1a-f, we show $V_{tg} - V_{bg}$ resistance maps for all six TBBG devices we measured. Extended Data Figures 1c-d are measured in the same TBBG sample, but in different sample regions that are approximately 27 µm apart (sections 1 and 2, respectively). Both regions have identical parameters (hence the two identical rows in table I), with the same twist angle θ=1.23°, and also nearly identical transport characteristics. The two sections are electrically disconnected via etching, but the extracted twist angles from the data have a difference of less than 0.01°, suggesting very uniform twist angles across this entire sample.

In almost all TBBG samples, we noticed a peculiar cross-like pattern around $(n, D) = (-n_s/2, 0)$, *i.e.* near p-side half-filling of the superlattice band. This is especially apparent in the 1.09° and 1.23° devices, which are highlighted in Extended Data Figures 1g-h. The p-side band does not exhibit a strong D-tunable correlated state as elaborated in the main text, possibly due to the larger bandwidth compared to its n-side counterpart. This cross-like pattern might represent an onset of correlated behaviour near half-filling of the band. Further experimental work and theoretical insight are needed to understand this phenomenon.

Sample quality and Landau fans

To demonstrate the high quality of our fabricated TBBG devices, we have measured the Landau fan diagrams and Hall mobilities of all three devices discussed in the main text, as shown in Extended Data Figure 2. The Hall mobilities are extracted from the ratio between the Hall coefficient R_H and longitudinal resistance at small magnetic fields (B<0.5 T). All three samples exhibit high Hall mobilities close to or above 100,000 cm^2/(V·s).

All three devices also show clear Landau fans starting from about 1 T. The filling factor of each level is labeled in the lower panels of each plot. In particular, due to the lower angle of the θ=0.84° device, its Landau fan displays a complicated Hofstadter's butterfly pattern starting from 3 T.

Linear R-T behaviour

Extended Data Figure 3 shows the resistance versus temperature behaviour, at different densities, observed across several small-angle TBBG devices. In the 1.23° device, we find approximately linear *R*-*T* behaviour above 10 K for densities ranging from 0.5~2.5×10^{12}cm^{-2}, encompassing the $n_s/2$ correlated state. The resistance slope in this range of densities does not vary very substantially, ranging from 210~350 Ω/K. Since all our devices have length-to-width ratios close to one, these slope values are therefore close to those reported in TBG[25,26]. In stark contrast, the resistance behaviour in the hole-doping side (n<0), as shown in Extended Data Figure 3b, shows qualitatively different behavior: it does not show linear *R*-*T* characteristics, at least up to 30 K, and the resistance value is about an order of magnitude smaller than on the electron-doping side. These data are consistent with the picture that the electron-doping band is flatter than the hole-doping band, therefore exhibiting more pronounced correlated phenomena, examples being the $n_s/2$ insulator state, and the linear resistance-temperature behaviour. Extended Data Figure 3c shows *R*-*T* curves close to the $n_s/2$ state.

The data for the 1.09° device shows a similar trend of linear *R*-*T* behaviour starting around 5~10 K, as shown in Extended Data Figure 3d.

In the 0.84° device, we find a very different behaviour. There is a region of sub-linear or approximately linear *R*-*T* behaviour at all densities, except at multiples of n_s, but the resistance slope is now strongly dependent on the charge density n. The slope approximately follows a power law $\frac{dR_{xx}}{dT} \propto n^a$ where $a \approx -1.77$ (see inset).

Theoretical Methods

The band structures shown in the main text are calculated using a continuum model based on the original continuum model for TBG [4,5], which qualitatively captures most of the important features of the bands in TBBG including displacement field dependence. To lowest order, the continuum model of twisted graphene superlattices is built on the approximation that the interlayer coupling between the A/B sublattice of one layer and the A/B sublattice of the other layer has a sinusoidal variation over the periodicity of the moiré pattern. For the three possible directions of interlayer connections between the wave vectors in the Brillouin zone, there are three connection matrices,

$$H_1 = w\begin{pmatrix}1 & 1\\1 & 1\end{pmatrix},$$

$$H_2 = w\begin{pmatrix} \omega^2 & 1 \\ \omega & \omega^2 \end{pmatrix},$$

$$H_3 = w\begin{pmatrix} \omega & 1 \\ \omega^2 & \omega \end{pmatrix},$$

where w is the interlayer hopping energy and $\omega = \exp(2\pi i/3)$. $H_{i,\alpha\beta}$, with $\alpha, \beta =$ A, B represents the hopping between sublattice α in the first layer to sublattice β in the second layer, with momentum transfer determined by i (see [4] for definition). Note that in this gauge choice, the origin of rotation is chosen where the B sublattice of the first layer coincides with the A sublattice of the second layer, so that the $H_{i,BA}$ component has zero phase while the other terms acquire phases. A different gauge choice is equivalent to an interlayer translation, which has been shown to have a negligible effect in the case of small twist angles [4,5].

To extend this formulation to TBBG, we add a simplified bilayer graphene Hamiltonian,

$$H_b = \begin{pmatrix} 0 & 0 \\ w_b & 0 \end{pmatrix}$$

between the non-twisted layers. The momentum transfer is zero since the bilayer is not twisted and the coupling is constant over the moiré unit cell. For simplicity, we only consider the 'dimer' coupling in the bilayer, neglecting second-nearest-neighbor hopping terms and trigonal warping terms. The two bilayers in TBBG (layer 1-2 and layer 3-4) have the same stacking order, *i.e.* for zero twist angle the total stacking would be 'ABAB' instead of 'ABBA'. In the calculations used in the main text, we used parameters $w = 0.1$ eV and $w_b = 0.4$ eV, so that when either parameter is turned off we obtain either the two non-interacting bilayer graphene ($w = 0$) or the non-interacting TBG and two monolayer graphene ($w_b = 0$).

Additional Magnetic Field Response Data

Extended Data Figure 4 shows the response of correlated states at $n_s/4$ and $3n_s/4$ in a perpendicular or in-plane magnetic field, similar to Fig. 3d-e, for the θ=1.23° device. For the $n_s/4$ state, we also find a signature of a phase transition at D/ε_0=-0.36 V/nm, manifesting as a shift of D-location of the correlated insulator as $B_\perp$ exceeds 6 T. The $3n_s/4$ state shows an overall monotonic increase of resistance and exhibits no shift of the position in D. In an in-plane field, on the other hand, as shown in Extended Data Figures 4b,d, both quarter filling states show a monotonic enhancement as $B_{\|}$ is increased, suggesting that they may have a similar spin-polarized ground state as the $n_s/2$ state.

I-V Curves and the Impact of Excitation Current on g-factor

In Extended Data Figure 5, we have plotted the *I-V* curves and differential resistance curves of the θ=1.23° device when it is in the correlated insulator states at $n_s/4$ and $n_s/2$. In the insulator states, we find a highly non-linear region near zero dc bias I_b=0 where the differential resistance $\mathrm{d}V_{xx}/\mathrm{d}I_b$ is significantly enhanced. This is in agreement with the existence of a small energy gap, which is overcome at higher bias voltages/currents. Outside of the insulator regions (such as shown in Extended Data Figure 5b), the *I-V* curves are mostly linear. For measuring the g-factors at $n_s/2$, we therefore used a much smaller excitation current of 0.1 nA in order to truthfully measure the differential resistance at I_b=0.

We wish to comment here on the effect of the ac excitation current on the measured gap sizes and the g-factor. When sourcing an ac bias current to measure the resistance using a lock-in technique, we effectively measure a weighted average of the differential resistance near zero bias. Due to the highly nonlinear *I-V* curve at the $n_s/2$ state, if the ac excitation is large, this average value will be much less than the peak value. Furthermore, the average value measured in this case can have a very different temperature dependence compared to the zero-bias value. For example, although to the best of our knowledge there is no detailed analysis of the high bias behaviour in the correlated insulator state of TBG, TBBG or related systems, if one considers the high bias transport to have contribution from a mechanism similar to Zener breakdown in semiconductors in an electrical field, the current is essentially independent of the temperature. There could be other contributions to the high bias transport as well, but in general their temperature dependence would not be identical to the zero-bias peak. In the Arrhenius fit that we use to extract the gap size, the gap size Δ is basically equal to how fast the resistance exponentially rises with T^{-1}. Therefore, a reduction of temperature dependence means that by averaging the higher bias differential resistance one would significantly underestimate the energy gap Δ, and so does the g-factor $g \sim \delta\Delta/\delta B$.

In Extended Data Fig. 6, we compare the Arrhenius fits of the resistance at $n_s/2$ and $n_s/4$ states, using a small excitation (0.1 nA) and a larger excitation (5~10 nA). We indeed find that by using an excessive excitation, both the gap size Δ and the g-factor are significantly underestimated. In particular, due to the larger nonlinearity at the $n_s/2$ state, its g-factor is underestimated by a factor of ~3 by using the larger excitation. Therefore, one should keep these nonlinear effects in mind when doing temperature dependent measurements on such resistive states to obtain accurate results.

Methods References

30. Pizzocchero, F. *et al.* The hot pick-up technique for batch assembly of van der Waals heterostructures. *Nat. Commun.* **7**, 11894 (2016).
31. Purdie, D. G. *et al.* Cleaning interfaces in layered materials heterostructures. *Nat. Commun.* **9**, 5387 (2018).
32. Wang, L. *et al.* One-Dimensional Electrical Contact to a Two-Dimensional Material. *Science* **342**, 614–617 (2013).

Data Availability

The data that support the findings of this study are available from the corresponding authors upon reasonable request.

Extended Data Tables

Extended Data Table 1. **List of TBBG devices discussed in the main text and Extended Data Figures.** The last device is marked with an asterisk to differentiate it from the first device, which happens to have the same twist angle but it is a totally independent device fabricated on a separate chip.

θ(°)	c_{tg}(F/m^2)	c_{bg}(F/m^2)	$V_{tg,0}$(V)	$V_{bg,0}$(V)	n_s(cm^{-2})
1.09	6.63×10^{-4}	5.02×10^{-4}	0.30	0.58	2.75×10^{12}
1.23	1.06×10^{-3}	7.14×10^{-4}	0.41	-0.04	3.55×10^{12}
1.23	1.06×10^{-3}	7.14×10^{-4}	0.41	-0.04	3.55×10^{12}
0.84	6.87×10^{-4}	6.38×10^{-4}	0.06	0.08	1.65×10^{12}
0.79	1.06×10^{-3}	3.57×10^{-4}	0.18	0.67	1.45×10^{12}
1.09(*)	1.03×10^{-3}	5.12×10^{-4}	0.28	0.45	2.75×10^{12}

Extended Data Figure Legends

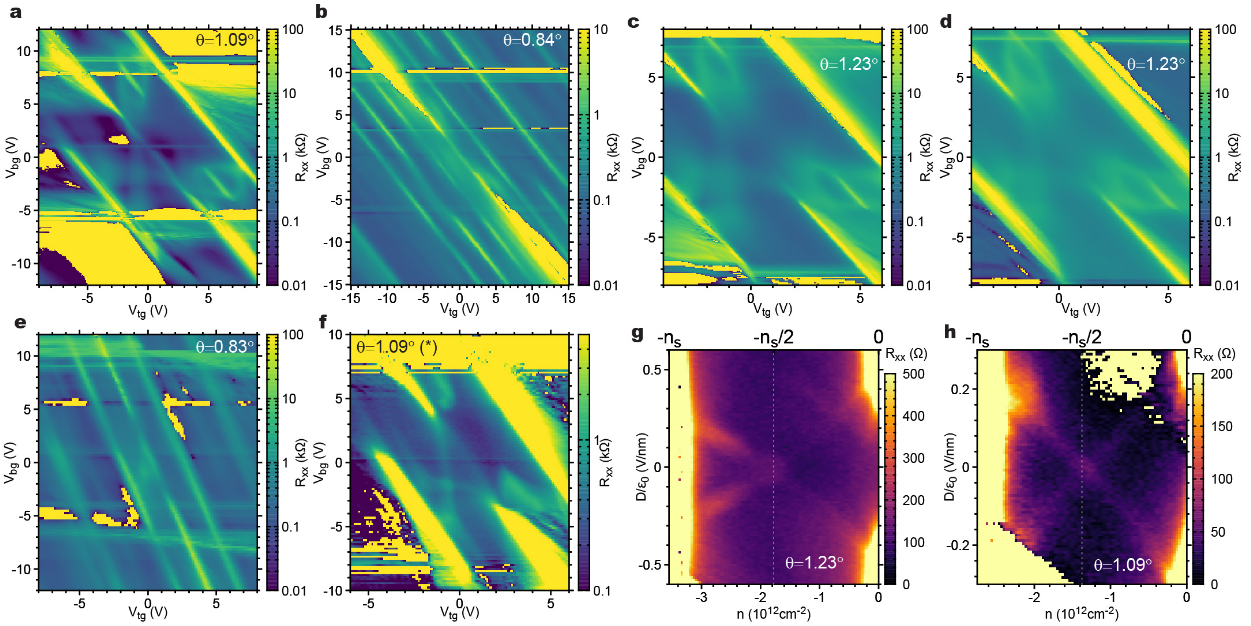

Extended Data Figure 1. ***V_{tg}*-*V_{bg}* resistance maps of measured TBBG devices.** (a-f) Resistance versus V_{tg} and V_{bg} for the six TBBG devices measured. (g-h) Cross-like feature near $-n_s/2$ in TBBG samples, which might signal the onset of a correlated state.

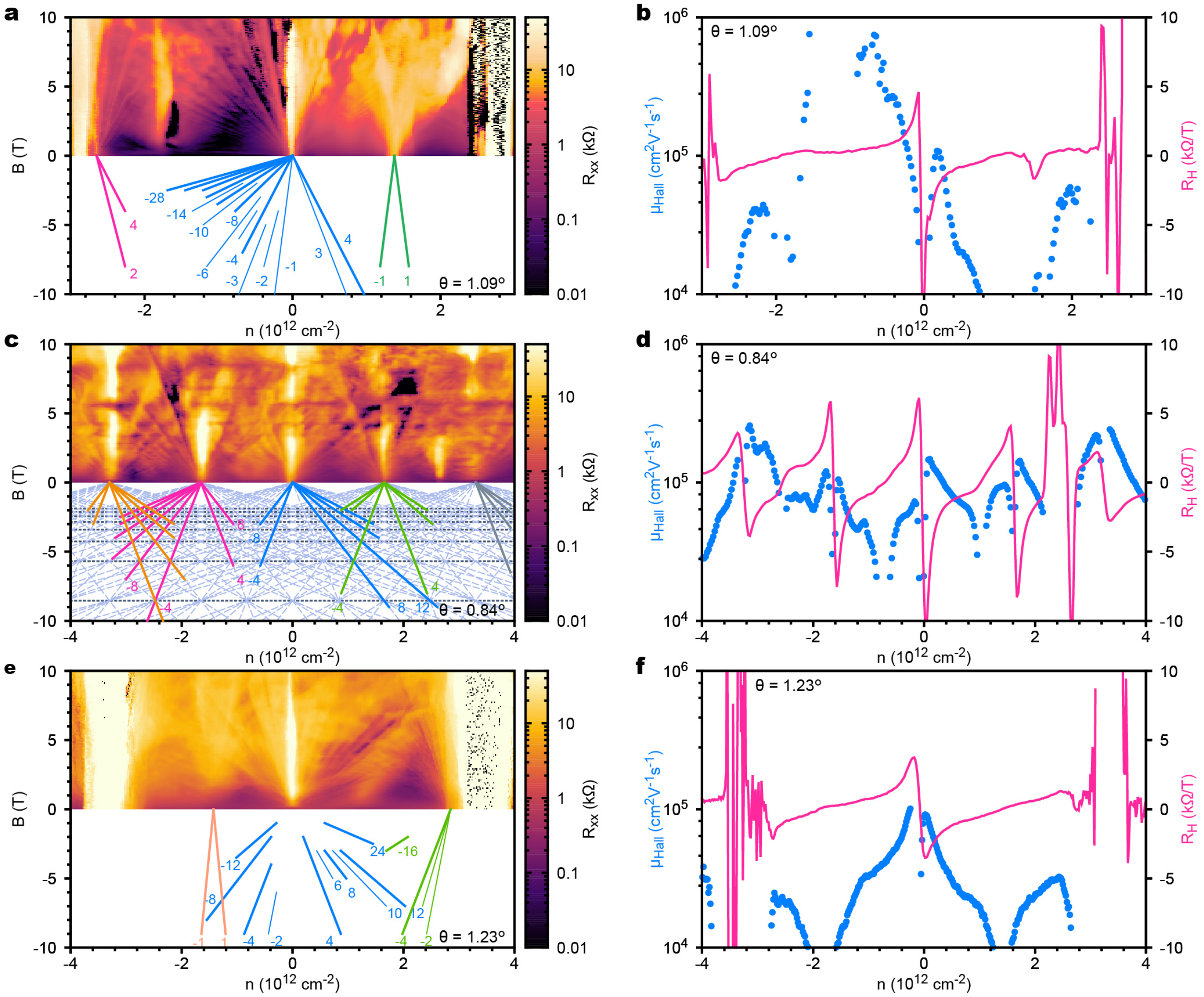

Extended Data Figure 2. **Landau fan diagrams and Hall mobilities of the TBBG devices.** (a) Resistance of the 1.09° sample versus carrier density and perpendicular magnetic field. (b) Hall mobility μ_{Hall} (left axis) and Hall coefficient R_H (right axis) in the 1.09° sample at different carrier densities. (c-f) Same measurements as in (a-b) but for the 0.84° and 1.23° samples, respectively. All measurements are taken at $T<100$ mK. The data for 1.09° device is taken at $D/\varepsilon_0=0.2$ V/nm while data for the other two devices are taken at $D=0$.

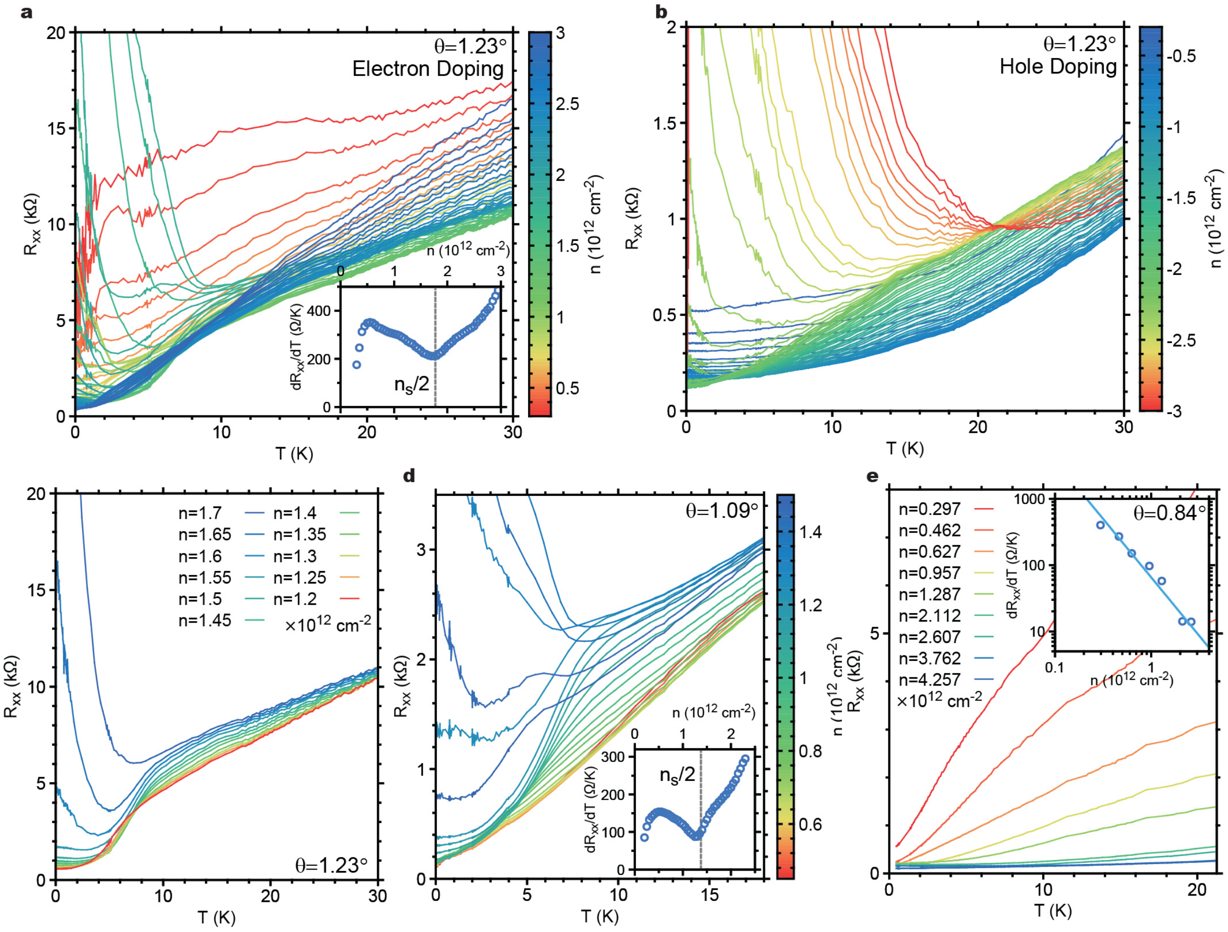

Extended Data Figure 3. **Linear resistance vs. temperature behaviour in TBBG**. (a-b) Resistance versus temperature curves at different charge densities in the 1.23° sample. Inset of (a) shows the slope dR_{xx}/dT of the linear R-T behaviour as a function of n for T>10 K. (c) Selected R-T curves near n_s/2 from (a). (d) Similar linear R-T behaviour in the 1.09° device. Inset shows the slope dR_{xx}/dT. (e) Density-dependent sublinear/linear R-T behaviour in the 0.84° device. Inset shows the slope dR_{xx}/dT versus n in log-log scale. The slope is proportional to n to the power of -1.77.

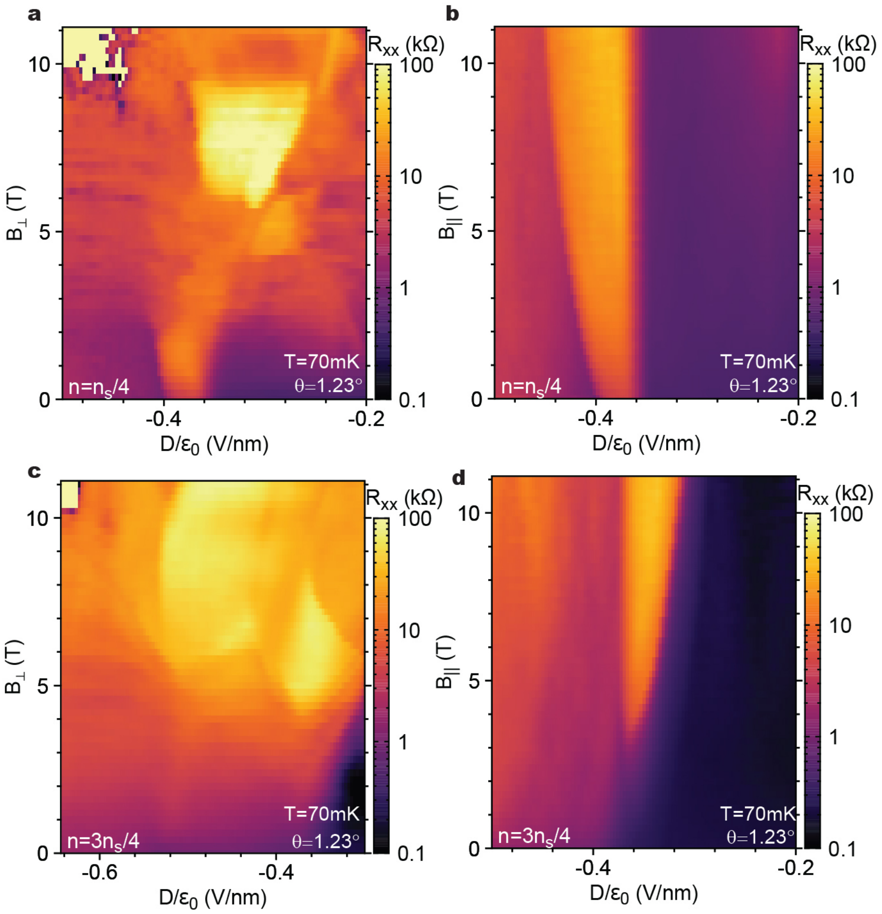

Extended Data Figure 4. **Additional magnetic field response of TBBG devices.** (a-d) Response of the $n_s/4$ and $3n_s/4$ states in perpendicular magnetic field and in-plane magnetic field.

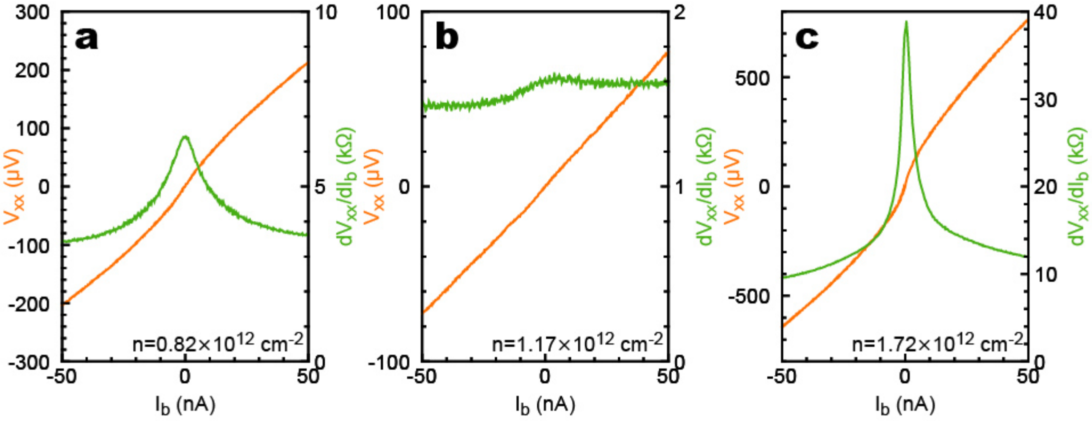

Extended Data Figure 5. ***I-V* curves in the 1.23° TBBG device at different carrier densities, $D/\varepsilon_0 = -0.38$ V/nm.** The densities of (a) and (c) correspond approximately to the $n_s/4$ and $n_s/2$ insulating states, respectively, while (b) lies in between them. Left axis is the longitudinal voltage V_{xx} and right axis is the differential resistance dV_{xx}/dI_b.

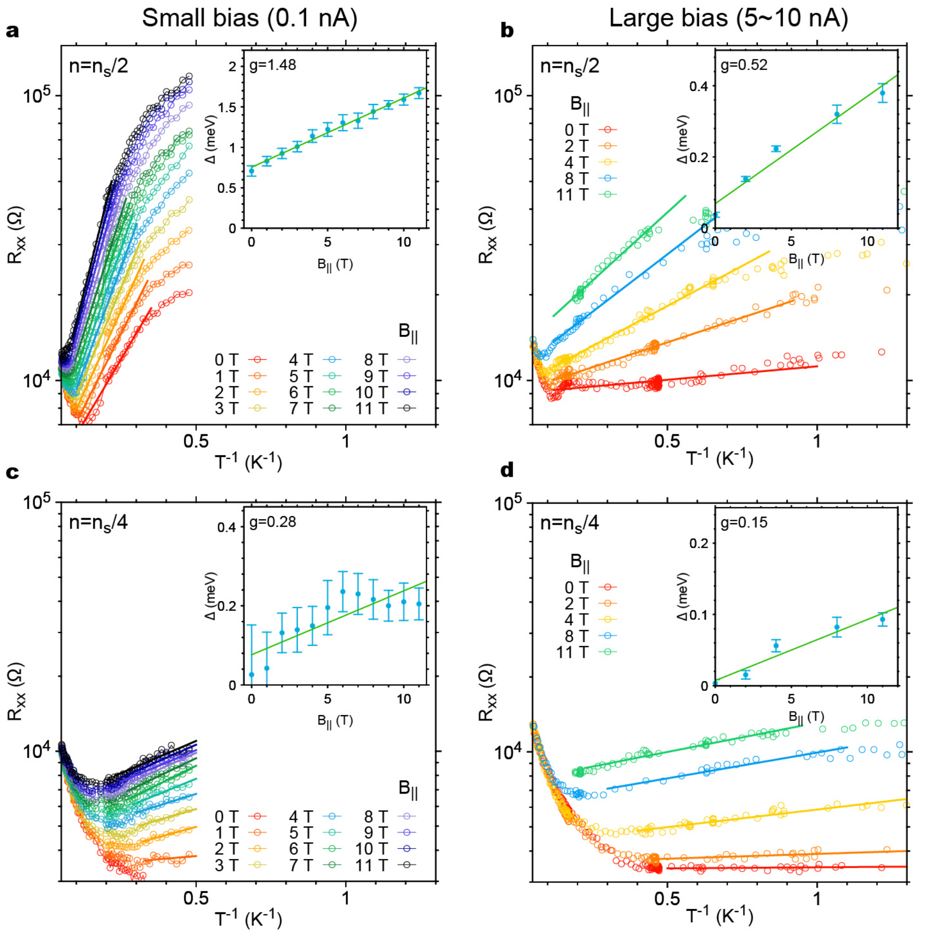

Extended Data Figure 6. **Comparison of the gap sizes and the g-factor using small excitation and large excitation.** (a-b) show the Arrhenius fits of the resistance at the $n_s/2$ state of the 1.23° TBBG device in an in-plane magnetic field and (c-d) show the same fits for the $n_s/4$ state. (a) and (c) are measured using a current excitation of 0.1 nA, while (b) and (d) are measured using a voltage excitation ~100 uV, which induces a current of 5~10 nA in the sample. The insets in each panel shows the corresponding g-factor fittings. In general, by using an excessive excitation, both the energy gaps and the *g*-factor will be underestimated.